High-pressure equation of state for Nb with a helium-pressure medium: Powder x-ray diffraction experiments

Takemura Kenichi*
National Institute for Materials Science (NIMS), Namiki 1-1, Tsukuba, Ibaraki 305-0044, Japan

Anil K. Singh
Materials Science Division, National Aerospace Laboratories, Bangalore 560 017, India
(Received 17 March 2006; revised manuscript received 22 May 2006; published 29 June 2006)

High-pressure powder x-ray diffraction experiments have been carried out on Nb at room temperature up to 134 GPa with a He-pressure medium and 145 GPa with an alcohol-water pressure medium. Nb remains in the bcc structure to the highest pressure investigated. The bulk modulus and its pressure derivative have been determined from the data with the He medium as $B_0=168(4)$ GPa and $B_0'=3.4(3)$. No anomaly is found in the equation of state of Nb to be connected with the electronic topological transitions, which were inferred from the anomalies in the superconducting transition temperature under pressure. The origin of the asymmetric broadening of the diffraction peaks is discussed.

DOI: 10.1103/PhysRevB.73.224119 PACS number(s): 64.30.+t, 62.20.Dc, 62.50.+p, 61.66.Bi

I. INTRODUCTION

Nb is a member of the 4*d* transition metals with bcc structure. The bulk modulus and its pressure derivative were determined by high-pressure powder x-ray diffraction,[1–3] ultrasonic,[4] and shock compression experiments.[5] The maximum pressure investigated was 60 GPa in the static experiment[3] and 174 GPa in the dynamic experiment.[5] In our recent x-ray diffraction study of Nb,[6] we have extended the static pressure range up to 145 GPa. The stress conditions in these measurements were, however, nonhydrostatic in the high-pressure region. It is now widely recognized that hydrostaticity is a key to get reliable values of bulk modulus and its pressure derivative.[7–10] The equation of state (EOS) forms the basis for a number of high-pressure studies. In order to determine the bulk modulus and its pressure derivative, we have carried out powder x-ray diffraction experiments on Nb under hydrostatic and quasihydrostatic conditions with a helium pressure-transmitting medium. Helium solidifies at about 12 GPa, but offers good quasihydrostatic conditions to at least 50 GPa.[11] The structural stability of the bcc phase is another interest of the study of Nb under high pressure. A total energy calculation suggests that the fcc structure will be stabilized for Nb at very high pressures.[12]

The effect of pressure on the superconducting transition temperature of Nb has been studied recently.[13] The study revealed two anomalies at 5 and 60 GPa: T_c jumps from 9 to 10 K at 5 GPa, remains nearly constant up to 60 GPa, and then falls off at higher pressures. These anomalies have been interpreted as electronic topological transitions (ETT's), which involve topological change of the Fermi surface at high pressures.[14] We have paid special attention to see whether any anomaly may appear in the EOS to be connected with the proposed ETT's. A preliminary account of the present work has been given elsewhere.[15]

II. EXPERIMENTS

A polycrystalline sample of Nb with stated purity of 99.9% obtained from Koch Chemicals Ltd. was finely ground in a mortar. The average particle size of the powder was less than 2 μm. In order to remove residual strain and to reduce possible hydrogen absorption,[16,17] the powdered sample was annealed at 700 °C in a vacuum for 1 h. The annealed sample was lightly pressed into a platelet, from which a tiny piece was cut and put in the gasket hole of the diamond-anvil cell (DAC). The typical size of the sample for the experiments to 100 GPa was about 3 μm in thickness and 30 μm in diameter. In some experimental runs, the sample powder was put in the gasket hole without pressing. We used spring steel gaskets for the experiments up to 20 GPa and Re gaskets for other experiments at higher pressures. Small ruby spheres (less than 5 μm in diameter) for pressure measurements were placed in several places in the gasket hole. Helium was loaded to the DAC at room temperature by using a high-pressure gas-loading system.[18] Pressures in the DAC were determined with the ruby luminescence method based on the pressure scale for the helium medium.[19] Comparison with the newly proposed ruby pressure scale[20] will be given in a later section. Eight experimental runs were carried out with the He medium. In addition, three runs were done with a methanol-ethanol-water (MEW) mixture in the volume ratio of 16:3:1 as the pressure medium. Pressure was determined with the nonhydrostatic ruby scale in this case.[21,22] Pressures were always measured before and after x-ray measurements.

Angle-dispersive powder x-ray diffraction experiments were carried out with an imaging plate[23] on the beamline BL-18C (bending magnet) and on the BL-13A (multipole wiggler) at the Photon Factory (PF), High Energy Accelerator Research Organization (KEK). The x-ray energy was 18–20 keV on BL-18C and 30 keV on BL-13A. The incident x-ray beam was collimated to the size of 80 μm in diameter for the experiments under hydrostatic and quasihydrostatic conditions up to 14 GPa. For the experiments at higher pressures, the beam size was reduced to 25–40 μm, depending on the pressure range. Typical exposure times were 10–50 min. The two-dimensional diffraction data were analyzed with the pattern integration software PIP.[24] All the

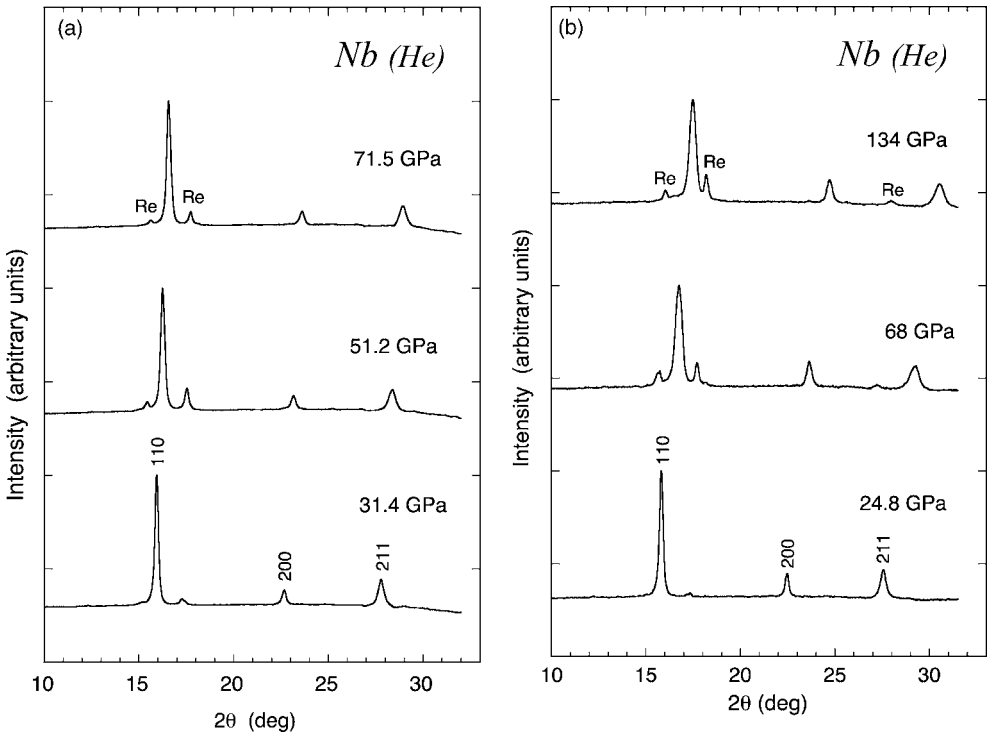

FIG. 1. Powder x-ray diffraction patterns of Nb at high pressures taken with the He pressure medium in two different runs. The x-ray wavelength was 0.6174 Å. Diffraction peaks from the Re gasket are indicated.

diffraction experiments were done at room temperature.

III. RESULTS

Figures 1(a) and 1(b) show two representative sets of x-ray diffraction patterns taken with He pressure medium. The diffraction peaks in (a) remain sharp in the entire pressure range, indicating good quasihydrostaticity. The lines in (b) show considerable broadening above 100 GPa. Figure 2 shows diffraction patterns with the MEW medium to the highest pressure achieved in this study. Although the peak broadening is significant, it is clear that Nb remains in the bcc structure to at least 145 GPa at room temperature. Table I lists the relative volume, lattice parameter, and d spacings as a function of pressure.

IV. DISCUSSION

A. Stress state of the sample

1. Qualitative assessment

Figure 3 compares the relative change in d spacings of Nb under pressure up to 20 GPa with He and MEW pressure media, where the d spacings are normalized to the values at atmospheric pressure d_0. The compression of each d spacing for the cubic system under hydrostatic pressure is independent of the indices hkl. This is seen to be the case for the data taken with He medium. For the MEW medium, however, the normalized d spacings above 9 GPa exhibit a dependence on hkl. This can be explained by the solidification of the MEW medium at high pressure and concomitant increase of the uniaxial stress component (USC). In such a case, the stress state of the sample is described by the superposition of the USC on the hydrostatic pressure, the direction of the USC being the direction of applied load in the DAC.[26] A crystal

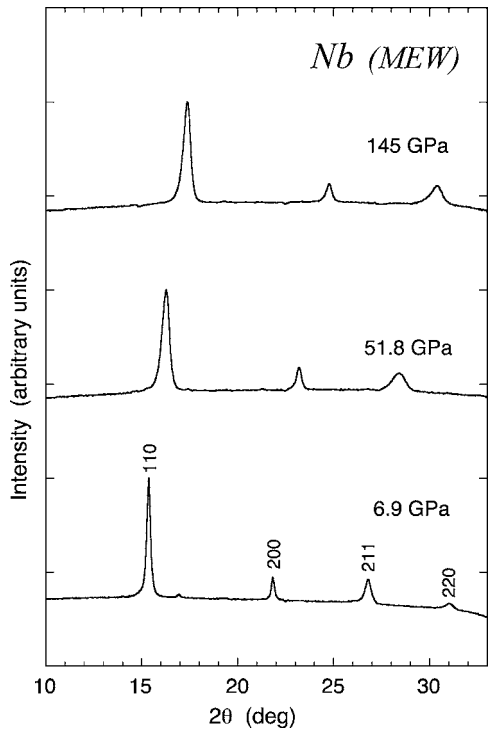

FIG. 2. Powder x-ray diffraction patterns of Nb at high pressures taken with the MEW pressure medium. The x-ray wavelength was 0.6180 Å.

TABLE I. Structural data of Nb under high pressure. The x-ray wavelength λ and uniaxial stress component t are also included in the table. The MEW pressure medium was used in run 1, while helium was used in other runs. The relative volume V/V_0 is calculated from the lattice parameter at atmospheric pressure [a=3.3007(3) Å] after Ref. 25. The error in P includes the difference of pressure among different ruby spheres and pressure change during x-ray measurements. Other errors shown in parentheses are from least-squares fits. Due to the large uniaxial stress component, run 11 was not used in the refinement of the bulk modulus.

Run	λ (Å)	P (GPa)	V/V_0	a (Å)	d_{110} (Å)	d_{200} (Å)	d_{211} (Å)	t (GPa)
1	0.6876	0.11(3)	0.9965(2)	3.2968(3)	2.3320(3)	1.6484(4)	1.3462(1)	0.15(3)
		0.74(3)	0.9950(1)	3.2952(1)	2.3303(1)	1.6476(2)	1.3454(1)	0.05(1)
		1.54(1)	0.9912(1)	3.2910(1)	2.3271(4)	1.6455(1)	1.3436(1)	0.01(1)
		2.55(13)	0.9854(1)	3.2846(1)	2.3230(2)	1.6423(4)	1.3411(1)	0.09(2)
		3.14(5)	0.9815(1)	3.2802(1)	2.3199(7)	1.6401(5)	1.3393(3)	0.09(2)
		3.77(3)	0.9784(1)	3.2768(1)	2.3171(2)	1.6384(7)	1.3378(7)	0.02(0)
		4.39(2)	0.9757(1)	3.2738(1)	2.3150(9)	1.6369(5)	1.3364(1)	−0.01(5)
		5.18(11)	0.9718(2)	3.2694(2)	2.3124(4)	1.6347(1)	1.3349(2)	0.11(4)
		5.75(15)	0.9695(1)	3.2668(1)	2.3102(1)	1.6334(3)	1.3336(1)	0.02(7)
		6.16(7)	0.9667(1)	3.2636(1)	2.3078(2)	1.6318(2)	1.3323(1)	0.00(3)
		6.66(10)	0.9636(1)	3.2602(1)	2.3054(3)	1.6301(3)	1.3310(1)	0.02(0)
		7.18(10)	0.9606(1)	3.2568(1)	2.3029(5)	1.6284(3)	1.3295(1)	−0.01(3)
		7.86(4)	0.9571(1)	3.2528(1)	2.3004(2)	1.6264(4)	1.3280(3)	0.05(5)
		8.88(2)	0.9520(2)	3.2470(2)	2.2968(6)	1.6235(3)	1.3257(2)	0.14(11)
5	0.6180	2.08(2)	0.9865(2)	3.2854(2)	2.3244(1)	1.6427(1)	1.3415(1)	0.20(15)
		5.26(2)	0.9699(4)	3.2652(5)	2.3096(2)	1.6326(2)	1.3340(1)	0.26(21)
		8.39(2)	0.9535(5)	3.2474(6)	2.2970(3)	1.6237(2)	1.3265(1)	0.22(13)
		11.32(3)	0.9400(3)	3.2324(4)	2.2871(2)	1.6162(2)	1.3201(1)	0.28(9)
		14.3(1)	0.9264(3)	3.2174(3)	2.2765(1)	1.6087(1)	1.3137(1)	0.24(20)
7	0.6198	2.3(1)	0.9820(4)	3.2808(4)	2.3234(1)	1.6404(2)	1.3415(3)	0.80(11)
		6.9(3)	0.9578(14)	3.2536(16)	2.3033(9)	1.6268(8)	1.3300(2)	0.65(12)
		12.1(1)	0.9361(2)	3.2288(2)	2.2850(16)	1.6144(1)	1.3199(1)	0.56(29)
		17.3(1)	0.9140(3)	3.2032(4)	2.2676(2)	1.6016(2)	1.3098(1)	0.72(29)
		22.1(2)	0.8981(3)	3.1846(4)	2.2561(3)	1.5923(2)	1.3020(1)	0.94(10)
		27.1(3)	0.8807(2)	3.1638(2)	2.2420(1)	1.5819(1)	1.2938(1)	1.10(12)
		32.6(2)	0.8636(10)	3.1432(12)	2.2268(7)	1.5716(6)	1.2863(2)	1.20(39)
		37.2(1)	0.8483(5)	3.1246(6)	2.2128(3)	1.5623(3)	1.2786(1)	1.06(53)
10	0.6174	31.4(2)	0.8618(16)	3.1412(20)	2.2264(1)	1.5706(10)	1.2856(3)	1.37(23)
		42.8(7)	0.8300(2)	3.1020(2)	2.2002(1)	1.5510(1)	1.2696(1)	1.69(0)
		51.2(8)	0.8090(2)	3.0756(2)	2.1826(7)	1.5378(1)	1.2599(14)	2.12(14)
		60.0(10)	0.7871(2)	3.0476(2)	2.1634(1)	1.5238(1)	1.2477(3)	2.15(32)
		68.3(2)	0.7698(5)	3.0252(6)	2.1473(12)	1.5126(3)	1.2388(1)	2.21(15)
		71.5(2)	0.7638(5)	3.0172(6)	2.1414(3)	1.5086(3)	1.2357(1)	2.23(3)
11	0.6174	24.8(5)	0.8849(10)	3.1690(12)	2.2435(9)	1.5845(6)	1.2958(3)	0.76(27)
		46.7(16)	0.8107(35)	3.0778(44)	2.1774(7)	1.5389(22)	1.2570(8)	0.27(1)
		57.6(21)	0.7832(20)	3.0426(26)	2.1427(1)	1.5213(13)	1.2370(12)	−2.51(30)
		68(3)	0.7609(8)	3.0134(10)	2.1192(4)	1.5067(5)	1.2235(4)	−3.48(44)
		83(4)	0.7344(4)	2.9780(6)	2.0956(11)	1.4890(3)	1.2099(4)	−3.20(41)
		94(5)	0.7173(6)	2.9548(8)	2.0807(8)	1.4774(4)	1.2000(11)	−3.08(105)
		104(6)	0.7026(3)	2.9344(4)	2.0662(13)	1.4672(2)	1.1923(5)	−3.06(72)
		115(7)	0.6880(4)	2.9140(6)	2.0520(12)	1.4570(3)	1.1845(3)	−2.97(53)
		126(8)	0.6748(3)	2.8952(4)	2.0398(10)	1.4476(2)	1.1769(1)	−2.80(81)
		134(9)	0.6667(1)	2.8836(2)	2.0312(15)	1.4418(1)	1.1722(1)	−2.93(70)

lattice under uniaxial stress deforms in such a way that the lattice planes lying perpendicular to the stress direction are compressed, whereas those lying parallel to the stress direction expand due to Poisson's effect.[27] This compression is

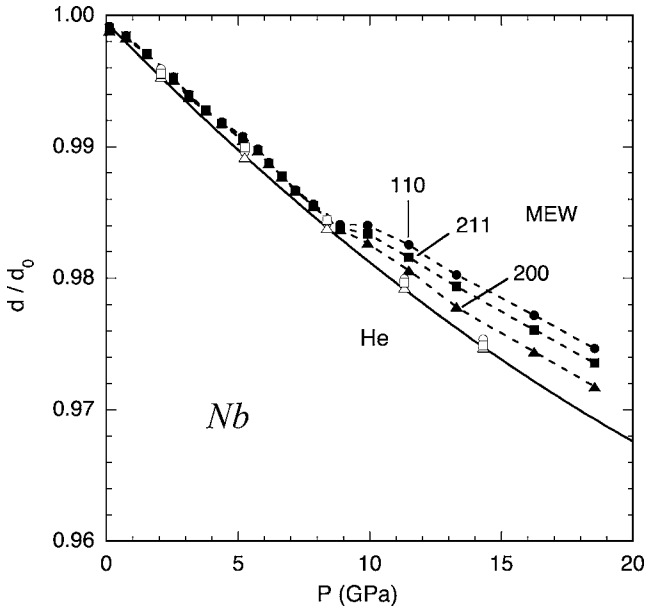

FIG. 3. Relative change of the d spacings of Nb as a function of pressure with a He (open symbols) and a MEW (solid symbols) pressure medium. Circles, triangles, and squares indicate the 110, 200, and 211 reflections, respectively. The experimental errors in d/d_0 and pressure are smaller than the size of the symbols.

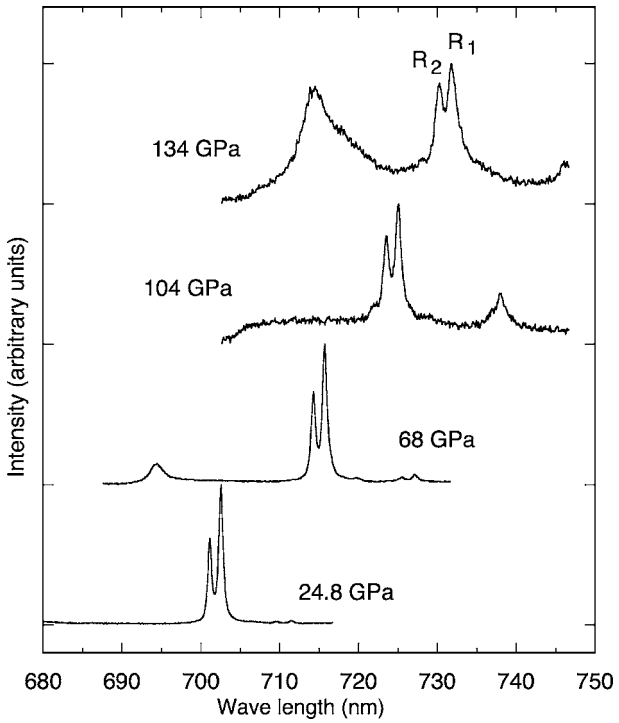

FIG. 4. Ruby luminescence spectra taken with the He pressure medium. Luminescence peaks other than R_1 and R_2 are getting strong at high pressures.

superimposed on the compression produced by the hydrostatic pressure. In the present diffraction geometry, the incident x-ray beam is parallel to the stress direction. It follows that the lattice planes, which lie nearly parallel to the load direction, selectively diffract x rays. The d spacings measured in such a case are larger than those under hydrostatic conditions. It is shown in the next section that the trend seen in Fig. 3 arises due to the onset of the USC and can be explained quantitatively on the basis of lattice strain theory. The MEW and He data shown in Fig. 3 slightly deviate even at pressures lower than 9 GPa, where the stress state is purely hydrostatic. This represents the overall accuracy of the present experimental method, which amounts to about $\pm 0.05\%$ in d spacings.

The diffraction lines in Fig. 1(b) above 100 GPa broaden considerably, indicating loss of quasihydrostaticity of He pressure medium. This is partly due to the small sample space, which is essential for reaching megabar pressures. The limited sample space makes it difficult to provide enough free space for the helium to surround the sample. Even if the sample is immersed in a helium pressure medium at low pressure, the high compressibility of helium results in a rapid reduction of volume as the pressure is increased. This results in the sample bridging the anvils. In the absence of bridging, nonhydrostaticity may set in because of the hardening of solid helium at ultrahigh pressures. In order to determine the EOS, the accuracy of pressure is as important as of the volume change of the sample. Figure 4 shows examples of ruby spectra taken in the He pressure medium. The R_1 and R_2 lines are well resolved at pressures up to nearly 70 GPa and gradually broaden at higher pressures. The broadening becomes appreciable by the time the pressure reaches 100 GPa. The shape and separation of the R_1 and R_2 lines give qualitative information on the hydrostaticity of the pressure.[28,29]

2. Quantitative evaluation

The stress state in the sample under nonhydrostatic compression in a DAC is axially symmetric.[30,31] The difference between the axial and radial stress components t, referred to as differential stress or USC in the preceding section, is a measure of nonhydrostaticity. Under truly hydrostatic pressure $t=0$ and in the absence of any pressure medium, the upper bound of t is limited by the compressive strength of the solid sample. The effect of such a stress state on the measured d spacings has been studied extensively.[26,30,32–34] For the cubic system, the lattice parameter $a_m(hkl)$ measured with the present diffraction geometry is given by

$$a_m(hkl) = M_0 + M_1[3(1 - 3\sin^2\theta)\Gamma(hkl)], \tag{1}$$

where

$$M_0 = a_P\{1 + (\alpha t/3)(1 - 3\sin^2\theta)[S_{11} - S_{12} - (1 - \alpha^{-1}) \times (2G_V)^{-1}]\}, \tag{2a}$$

$$M_1 = -a_P\alpha t S/3, \tag{2b}$$

$$\Gamma(hkl) = (h^2k^2 + k^2l^2 + l^2h^2)/(h^2 + k^2 + l^2)^2, \tag{2c}$$

$$S = S_{11} - S_{12} - S_{44}/2. \tag{2d}$$

It follows from Eqs. (2a) and (2b) that, to a good approximation,

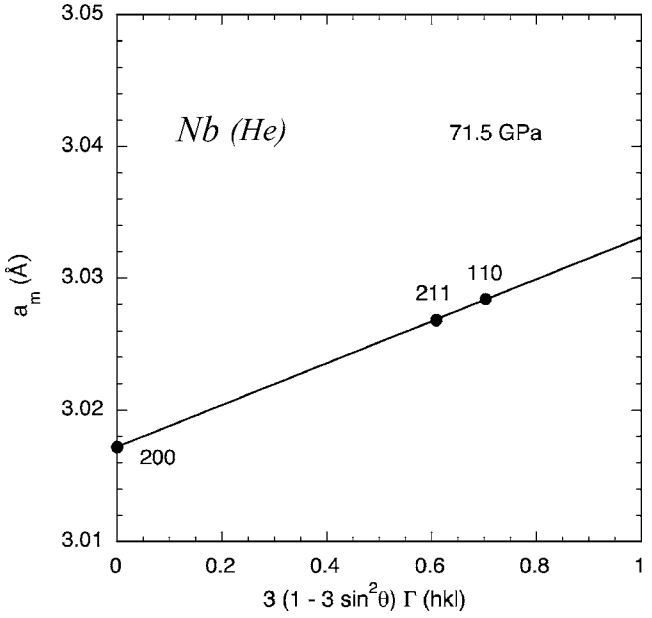

FIG. 5. The gamma plot for Nb with a He pressure medium at 71.5 GPa. The lattice parameters a_m calculated from each reflection are plotted as a function of $3\ (1-3\sin^2\theta)\Gamma(hkl)$. See text for the detailed explanation.

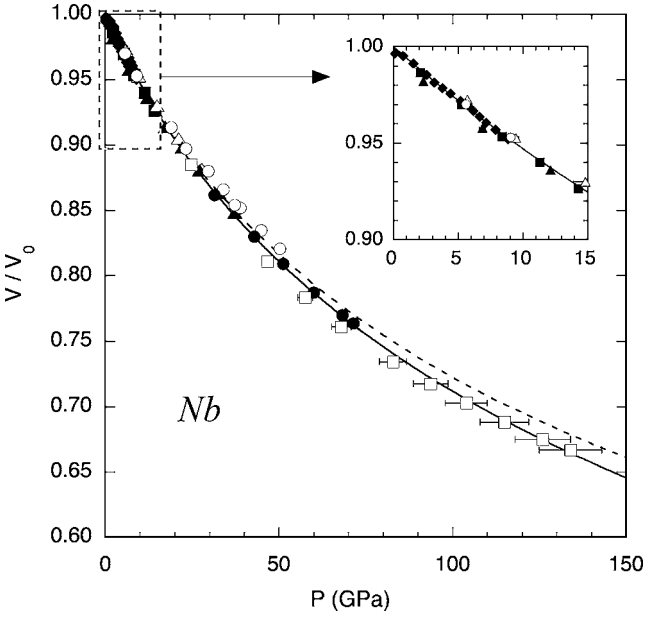

FIG. 6. Pressure-volume relationship of Nb. Different symbols show different experimental runs in the present experiments. Solid symbols are the best data, which are used to obtain the bulk modulus. The solid curve is a fit with the Burch-Murnaghan EOS with $B_0=168$ GPa and $B_0'=3.4$. The dashed curve is the shock compression data reduced to $T=0$ K (Ref. 5). The inset shows an enlarged plot at low pressures.

$$t \cong -\frac{3M_1}{\alpha M_0 S}. \tag{3}$$

a_P is the lattice parameter under equivalent hydrostatic pressure that equals the mean normal stress, S_{ij} denote the single-crystal elastic compliances, and G_V is the shear modulus of the polycrystalline aggregate under the assumption of strain continuity across the boundaries separating the crystallites. The parameter α decides the actual stress state of the sample that is assumed to lie between the two extreme conditions of stress and strain continuity across the boundaries separating the crystallites. The derivation of these equations is given elesewhere.[6] It can be also shown[6] that a plot of $a_m(hkl)$ versus $3(1-3\sin^2\theta)\Gamma(hkl)$, termed the gamma plot, is a straight line. A typical gamma plot is shown in Fig. 5. The t values calculated using Eq. (3) with $\alpha=1$ for each run are shown in Table I. The assumption of $\alpha=1$ gives the lower bound of t. The single-crystal elastic compliances at high pressures required in Eq. (3) were calculated with Birch equations[35] using the one-atmosphere single-crystal elastic moduli and their pressure derivatives obtained from ultrasonic measurements.[4]

It is seen that t tends to increase with increasing pressure and reaches 2.2 GPa at 71.5 GPa. The sample bridging of the anvils and hardening of the pressure medium are two factors, which can render the stress state nonhydrostatic and give rise to nonzero t. If it is assumed that bridging does not occur, then the t values listed in Table I represent the strength of solid He. These values are comparable to a strength of 2.5(5) GPa of solid argon at 55 GPa found in a recent study.[36] The data of run 11, except at the first two pressures, give negative t. A negative t would imply that the radial stress component was larger than the axial stress component. Small negative t can arise due to the scatter in the data, as is the case at 4.39 and 7.18 GPa of run 1. Large negative t values are not commonly observed but, in principle, can arise if the sample chamber collapses on application of load. Optical examination of the high-pressure cell assembly indicated that the gasket had deformed and shifted slightly from the center of the anvils. Some portions of the gasket hole were optically clear, indicating that He was still contained in the gasket. Three ruby spheres ($\sim 3\ \mu$m in diameter) also showed a large pressure difference above 70 GPa. It was difficult to assess if the collapse of the gasket hole was adequate to give rise to large negative t. In view of this uncertainty and presence of large t, the data of run 11 were not considered in calculations of the compression parameters.

In the entire pressure range, S for Nb remains negative.[6] A simple manipulation of Eq. (1) suggests that the nonhydrostatic compression effect for negative S is largest for 110 and least for 200 reflection, a trend evident in Fig. 3. To minimize the errors caused by the neglect of nonhydrostatic compression effect, the d spacing of only 200 was used to compute the unit cell volume. Figure 6 shows the pressure-volume relationship thus obtained. Different symbols correspond to different experimental runs. The best data are shown by solid symbols, which are slightly more compressible than the reduced shock-wave data. The estimated maximum error in the cell volume at 71.5 GPa is $\sim 0.5\%$ and decreases at lower pressures.

B. Equation of state

The bulk modulus B_0 and its pressure derivative B_0', both at atmospheric pressure, are determined by fitting the present

TABLE II. Bulk modulus and its pressure derivative of Nb. The pressure range used in the analysis, methods of investigation, pressure medium, and pressure scale are indicated. Values of B_0' in square brackets mean that they were assumed in the analysis.

B_0 (GPa)	B_0'	P (GPa)	Method	Pressure medium	Pressure scale (Ref.)	Ref.
168(4)	3.4(3)	0–72	X-ray	He	20	Present work
168(4)	3.6(3)	0–72	X-ray	He	20	Present work
171(7)	[4.03]	0–10	X-ray	ME[a]	38	1
175.7(27)	[4]	0–60	X-ray	Water	21	2
168	3.25	0–60	X-ray	Gold	39	3
161(1)	3.2(1)	0–50	X-ray	MEW, He	21	6
168.98	4.08	0–0.5	Ultrasonic	Nitrogen		4
168.8(3)	3.73(1)	0–174	Shock wave			5
165	3.45	0–250	Theory			40

[a]Methanol-ethanol mixture in the volume ratio of 4:1.

pressure-volume data with the Birch-Murnaghan EOS. The relative volume at atmospheric pressure was fixed to 1 in the fitting procedure. If we fit the best quasihydrostatic data up to 71.5 GPa, we obtain $B_0=167.9\pm1.7$ GPa and $B_0'=3.45\pm0.10$. If we use all the data up to 134 GPa (excluding the MEW data above 9 GPa), we obtain $B_0=171.5\pm3.0$ GPa and $B_0'=3.28\pm0.11$. By considering the uncertainty in pressure and volume determination above 100 GPa, we adopt the former values of B_0 and B_0', attaching error bars spanning the two determinations as $B_0=168\pm4$ GPa and $B_0'=3.4\pm0.3$. A fit to the Vinet formula for the EOS (Ref. 37) yields a slightly smaller value for B_0 and a larger value for B_0', but the differences from the fit with the Birch-Murnaghan EOS are well within the error bars. The B_0 and B_0' values are compared with previous determinations in Table II and plotted in Fig. 7. The present result is in close agreement with the data by Akahama *et al.*[3] It is also in reasonable agreement with a theoretical calculation,[40] which employed the full-potential linear muffin-tin orbital (LMTO) method with the generalized gradient approximation. In our preceding work,[6] we applied corrections for the USC on the diffraction data of Nb taken under nonhydrostatic conditions and evaluated the lattice constants under hydrostatic conditions. The obtained bulk modulus (161 GPa) is 7 GPa smaller than the present one, while the value without correction (183 GPa) is 15 GPa larger. The B_0' value is close to the present one, irrespective of the correction. This may represent the limitation of using nonhydrostatic data and correcting for the effect of the USC. Uncertainty in pressure could be another source of deviation of the EOS obtained under nonhydrostatic conditions.

One notices in Fig. 7 that B_0 is nearly the same for the present and most previous experiments (168-171 GPa), while B_0' in the present work is much smaller than the values from ultrasonic and shock compression measurements. There are discussions on the validity of the ruby pressure scale in the 100 GPa range. Dewaele *et al.* have recently proposed an updated ruby pressure scale based on the comparison of the EOS of several metals.[20] If we use their updated scale, pressure values increase by about 4.3 GPa at 100 GPa. Consequently, we obtain the values $B_0=168\pm4$ GPa and $B_0'=3.6\pm0.3$, which are in excellent agreement with the shock-wave data.[5] In other words, the present experimental data on Nb give support to the updated ruby pressure scale, provided that the B_0' value from the shock-wave experiments is reliable.

C. Electronic topological transitions

After the report on the pressure dependence of the superconducting transition temperature,[13] energy band calculations have been done on Nb to see the change in the topology of the Fermi surface under pressure.[41–43] The first two calculations support the existence of an ETT in Nb at around 60 GPa, while the ETT at lower pressure is ambiguous. Os-

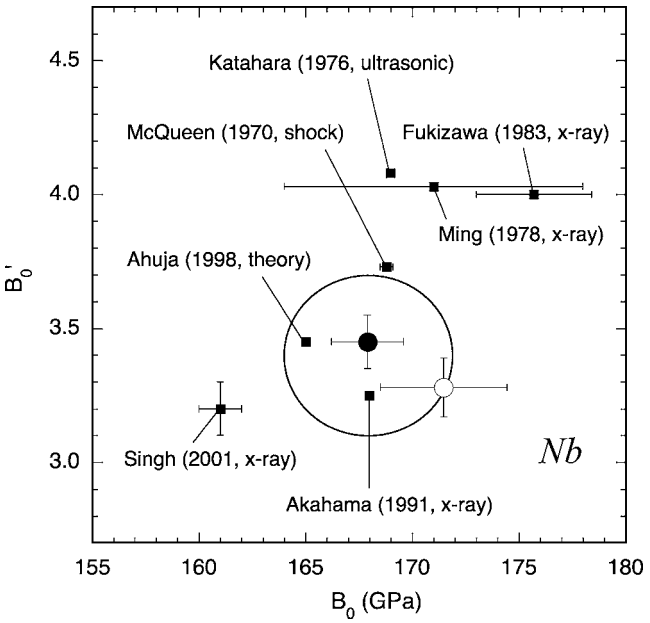

FIG. 7. Bulk modulus B_0 and its pressure derivative B_0' for Nb. Solid and open circles indicate the present results for pressure range 0–72 GPa, and 0–134 GPa, respectively. The large ellipsoid, which encloses the solid and open circles, indicates the probable range of the values B_0 and B_0' determined in the present experiments. Previous experimental and theoretical data are shown by solid squares.

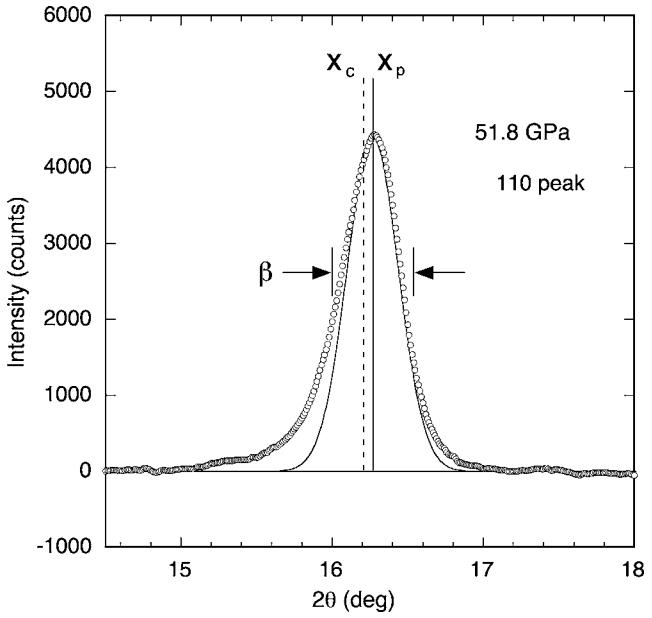

FIG. 8. The 110 diffraction peak of Nb at 51.8 GPa taken with the MEW pressure medium. Background intensity is subtracted. The positions of peak intensity x_P and the centroid x_C are indicated by solid and dashed vertical lines, respectively. The integral width β is also indicated. The asymmetric peak profile is evident, if one compares the observed profile (open circles) with a fit with a Gaussian function (solid curve). The x-ray wavelength was 0.6180 Å.

tanin *et al.* found no change in the band structure in the low-pressure region.[41] On the other hand, Tse *et al.* found a subtle change in the Hall coefficient at around 5 GPa, which they ascribed to the anomaly in T_c.[42] Landa *et al.* reported that the calculated elastic constant C_{44} showed softening at around 50 GPa.[43] In the present experiments, we have observed no detectable anomalies in the EOS at 5 and 60 GPa at room temperature (Fig. 6 and inset). Of course, it is not clear whether the ETT's may induce structural anomalies, as suggested for Zn under pressure.[27,44–46] High-pressure diffraction experiments at low temperature are also important to directly compare the structural change with the measured electron transport properties.

D. Asymmetric peak broadening

One of the remarkable observations in the present experiments is the asymmetric broadening of the diffraction peaks of Nb at high pressures, specifically when the MEW pressure medium was used (Fig. 2). Figure 8 displays the enlarged view of the 110 peak at 51.8 GPa.

The nonhydrostatic compression leads to a reduction in the particle size and the appearance of micro strains. These factors lead to diffraction-line broadening[47] and, to a good approximation, do not affect the line position. It has been known for quite some time (for example, see Ref. 48) that the broadening depends, among other factors, on $1/E(hkl)$, where $E(hkl)$ is Young's modulus along the direction $[hkl]$. Recently, this dependence was shown to be valid also for the widths of diffraction lines recorded at high pressure.[49]

Line broadening caused solely by the single-crystal elastic anisotropy has been discussed recently.[49,50] The theory predicts the absence of broadening from this source for reflections of the type *hhh* and *h*00. Further, the broadening is asymmetric for some diffraction geometry. The three diffraction lines (110, 200, and 211) recorded in the present study were well separated. The intensity data were recorded at 0.01° (2θ) intervals. The peak-to-background ratio was ~2.5 for 110 reflection and ~1.3 for 200 and 211 reflections. The quality of the diffraction data is typical of good high-pressure data but certainly poor when compared with data commonly employed for line-profile studies. Therefore, a large uncertainty in the results in this section is not surprising. The background intensity was fitted to a polynomial and the intensities computed from this polynomial were subtracted from the observed intensities. The background was found to be reasonably flat on either sides of the 110 and 200 lines. The 211 line, being close to the end of the recording area of the image plate, had a highly nonlinear background on the larger 2θ side. The intensity of the diffraction line was assumed to be fully included within a region of 1.5° on either side of the peak. The position of the centroid (mean) was calculated by the following relation:

$$x_C = \int_{x_1}^{x_2} xI(x)dx \Big/ \int_{x_1}^{x_2} I(x)dx, \tag{4}$$

where $x=2\theta$, $I(x)$ is the intensity at x, and $x_1=x_C-1.5°$ and $x_2=x_C+1.5°$. The second moment about x_C (variance) is given by

$$\sigma^2 = \int_{x_1}^{x_2} (x-x_C)^2 I(x)dx \Big/ \int_{x_1}^{x_2} I(x)dx. \tag{5}$$

The Karl Pearson measure of skewness[51] (asymmetry) is dimensionless quantity and is given by

$$S = (x_C - x_P)/\sigma, \tag{6}$$

where x_P is the position of peak intensity $I(x_P)$. The integral width of the diffraction line is defined by

$$\beta = \int_{x_1}^{x_2} I(x)dx/I(x_P). \tag{7}$$

For the reasons discussed below we use slightly modified measure of skewness (asymmetry) in the present discussion,

$$A = (x_C - x_P)/\beta. \tag{8}$$

The parameters given by Eqs. (4)–(8) were numerically computed. The σ^2 computed from Eq. (5) was found to be sensitive to choice of background level and the range of integration. This was the major source of uncertainty in the computation of S. Sacrificing mathematical rigor, we used the asymmetry parameter A given by Eq. (8) rather than the mathematically correct measure S. In a typical case, a decrease of 1% in background level resulted in a decrease of ~ 7% in A but S decreased by ~22%. The two measures of width, σ and β, are related for a given intensity distribution in the profile. Since $\beta > \sigma$ for commonly recorded profiles, $|A| < |S|$. It may be noted that the third moment about x_C is

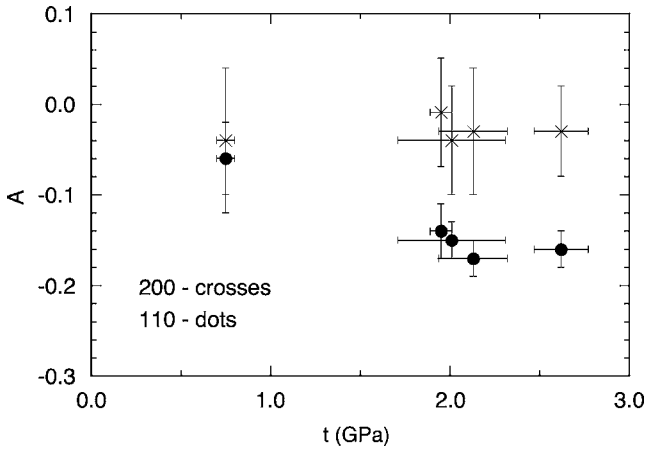

FIG. 9. The asymmetry parameter A as a function of the uniaxial stress component t for the data taken with the MEW pressure medium. See text for the explanation of A.

related to S and directly gives the skewness. This parameter was not used because the third moment is even more sensitive (than the second moment) to the uncertainties in the background level and the range of integration.

The asymmetry parameters for all three reflections are small when the pressure is hydrostatic as judged from the analysis given earlier.[6] For the nonhydrostatic compression, the 110 and 211 reflections exhibit appreciable asymmetry but the 200 reflection remains symmetric. This trend is seen in the A versus t plot for 200 and 110 reflections (Fig. 9). The t values in this plot are from our earlier study.[6] The A values for 211 reflections are close to those for 110. The scatter is much larger as compared to the scatter in 110 mainly because of larger errors in the background estimation. For sake of clarity, data for 211 are not shown in Fig. 9. Two trends are clearly seen: A for 200 is small and practically independent of t, and the magnitude of A for 110 increases with increasing t. This trend is predicted from the theory.[49,50] It appears possible to estimate t measured from the asymmetry parameter A for different reflections. However, it may be noted that the asymmetry of the line is a higher-order effect and not always observed. Even when it is observed, the estimation of t from A values will have large uncertainties. Reliable estimates of t can be obtained from the analysis of β or any other equivalent measure of line width (see, e.g., Ref. 52).

Of the other sources of asymmetric broadening, effects of the radial pressure gradient and deformation twins are important. It is shown recently[53] that the pressure gradient in the sample region illuminated by the primary beam by itself does not cause asymmetric broadening. However, the asymmetry in the peak arises if the primary beam with a nonuniform intensity distribution passes through the region of the pressure gradient. In such a case, all the reflections will develop asymmetry. This does not explain the present observation that the 200 reflection remains symmetric. The deformation twins are known to produce asymmetric broadening in a face-centered-cubic system but the effect is extremely small in a body-centered-cubic system.[54] The calculated powder diffraction pattern for bcc crystals containing stacking faults on the (211) planes shows a much larger integral width for the 200 reflection than for other reflections,[55] which contradicts the present observation. The asymmetry is undoubtedly caused by t. A quantitative comparison will require profiles recorded with much improved precision.

V. CONCLUSION

The analysis of the compression data on Nb taken with He pressure medium indicates the presence of a uniaxial stress component that is small at low pressures and increases with increasing pressure, reaching 2.23(3) GPa at 71.5 GPa. It appears difficult to achieve better hydrostaticity as the nonhydrostatic effect most likely results from the strength of the He pressure medium. A value of 2.23(3) GPa for the strength of solid He at 71.5 GPa compares well with the strength of 2.5(5) GPa of solid argon at 55 GPa determined recently. The bulk modulus and its pressure derivative of Nb at one atmosphere obtained from the present compression data are in good agreement with those reported earlier. The body-centered-cubic phase of Nb is stable to at least 145 GPa.

ACKNOWLEDGMENTS

The authors thank T. Kikegawa, K. Sato, and S. Nakanao for their help in the experiments at the Photon Factory. They also thank T. Matsumoto for annealing the Nb sample and R. Ahuja for communicating his results. Useful discussions with M. Arai and K. Kobayashi are gratefully acknowledged. The present work has been done under Proposals No. 97G269, No. 99G204, No. 00G210, and No. 01G225 of the Photon Factory. A.K.S. thanks the Director, NAL, for supporting this research activity.

*Electronic address: takemura.kenichi@nims.go.jp

[1] L-c. Ming and M. H. Manghnani, J. Appl. Phys. **49**, 208 (1978).
[2] A. Fukizawa and Y. Fukai, J. Phys. Soc. Jpn. **52**, 2102 (1983).
[3] Y. Akahama, M. Kobayashi, and H. Kawamura, J. Phys. Soc. Jpn. **60**, 3211 (1991).
[4] K. W. Katahara, M. H. Manghnani, and E. S. Fisher, J. Appl. Phys. **47**, 434 (1976).
[5] R. G. McQueen, S. P. Marsh, J. W. Taylor, J. N. Fritz, and W. J. Carter, in *High Velocity Impact Phenomena*, edited by R. Kinslow (Academic Press, New York, 1970), p. 293.
[6] A. K. Singh and K. Takemura, J. Appl. Phys. **90**, 3269 (2001).
[7] J. W. Otto, J. K. Vassiliou, and G. Frommeyer, Phys. Rev. B **57**, 3253 (1998).
[8] S. Speziale, C.-S. Zha, T. S. Duffy, R. J. Hemley, and Ho-kwang Mao, J. Geophys. Res. **106**, 515 (2001).
[9] K. Takemura, Phys. Rev. B **70**, 012101 (2004).

[10] A. Dewaele, P. Loubeyre, and M. Mezouar, Phys. Rev. B **69**, 092106 (2004).
[11] K. Takemura, J. Appl. Phys. **89**, 662 (2001).
[12] R. Ahuja, P. Söderlind, J. Trygg, J. Melsen, J. M. Wills, B. Johansson, and O. Eriksson, Phys. Rev. B **50**, R14690 (1994).
[13] V. V. Struzhkin, Y. A. Timofeev, R. J. Hemley, and Ho-kwang Mao, Phys. Rev. Lett. **79**, 4262 (1997).
[14] I. M. Lifshitz, Zh. Eksp. Teor. Fiz. **38**, 1569 (1960) [Sov. Phys. JETP **11**, 1130 (1960)].
[15] K. Takemura, in *Science and Technology of High Pressure, Proceedings of AIRAPT-17, Hawaii, 1999*, edited by M. H. Manghnani, W. J. Nellis, and M. F. Nicol [Universities Press (India), Hyderabad, 2000], p. 443.
[16] A. Magerl, B. Berre, and G. Alefeld, Phys. Status Solidi A **36**, 161 (1976).
[17] M. A. Pick and R. Bausch, J. Phys. F: Met. Phys. **6**, 1751 (1976).
[18] K. Takemura, P. Ch. Sahu, Y. Kunii, and Y. Toma, Rev. Sci. Instrum. **72**, 3873 (2001).
[19] C-S. Zha, Ho-kwang Mao, and R. J. Hemley, Proc. Natl. Acad. Sci. U.S.A. **97**, 13494 (2000).
[20] A. Dewaele, P. Loubeyre, and M. Mezouar, Phys. Rev. B **70**, 094112 (2004).
[21] H. K. Mao, P. M. Bell, J. W. Shaner, and D. J. Steinberg, J. Appl. Phys. **49**, 3276 (1978).
[22] For the MEW pressure medium, the ruby luminescence became very weak above 100 GPa due to the large nonhydrostatic stresses. In this case, the pressure was estimated from the *d* spacings of the Re gasket calculated from the equation of state given by Y. K. Vohra, S. J. Duclos, and A. L. Ruoff, Phys. Rev. B **36**, 9790 (1987). The estimated uncertainty in pressure was ±5–10 GPa for this method.
[23] O. Shimomura, K. Takemura, H. Fujihisa, Y. Fujii, Y. Ohishi, T. Kikegawa, Y. Amemiya, and T. Matsushita, Rev. Sci. Instrum. **63**, 967 (1992).
[24] H. Fujihisa (unpublished).
[25] J. Donohue, *The Structures of the Elements* (Wiley, New York, 1974), p. 179.
[26] A. K. Singh and G. C. Kennedy, J. Appl. Phys. **45**, 4686 (1974).
[27] K. Takemura, Phys. Rev. B **60**, 6171 (1999).
[28] G. J. Piermarini, S. Block, and J. D. Barnett, J. Appl. Phys. **44**, 5377 (1973).
[29] M. Chai and J. M. Brown, Geophys. Res. Lett. **23**, 3539 (1996).
[30] A. K. Singh, C. Balasingh, H. K. Mao, R. J. Hemley, and J. Shu, J. Appl. Phys. **83**, 7567 (1998).
[31] A. L. Ruoff, J. Appl. Phys. **46**, 1389 (1975).
[32] A. K. Singh, J. Appl. Phys. **73**, 4278 (1993).
[33] T. Uchida, N. Funamori, and T. Yagi, J. Appl. Phys. **80**, 739 (1996).
[34] A. K. Singh, H. K. Mao, J. Shu, and R. J. Hemley, Phys. Rev. Lett. **80**, 2157 (1998).
[35] F. Birch, J. Geophys. Res. **83**, 1257 (1978).
[36] Ho-kwang Mao, J. Badro, J. Shu, R. J. Hemley, and A. K. Singh, J. Phys.: Condens. Matter **18**, S963 (2006).
[37] P. Vinet, J. Ferrante, J. H. Rose, and J. R. Smith, J. Geophys. Res. **92**, 9319 (1987).
[38] G. J. Piermarini, S. Block, J. D. Barnett, and R. A. Forman, J. Appl. Phys. **46**, 2774 (1975).
[39] J. C. Jamieson, J. N. Fritz, and M. H. Manghnani, in *High Pressure Research in Geophysics*, edited by S. Akimoto and M. H. Manghnani (Center for Academic Publications Japan, Tokyo, 1982), p. 27.
[40] R. Ahuja (private communication).
[41] S. A. Ostanin, V. Yu. Trubitsin, S. Yu. Savrasov, M. Alouani, and H. Dreyssé, Comput. Mater. Sci. **17**, 202 (2000).
[42] J. S. Tse, Z. Li, K. Uehara, Y. Ma, and R. Ahuja, Phys. Rev. B **69**, 132101 (2004).
[43] A. Landa, J. Klepeis, P. Söderlind, I. Naumov, O. Velikokhatnyi, L. Vitos, and A. Ruban, J. Phys.: Condens. Matter **18**, 5079 (2006).
[44] Zhiqiang Li and J. S. Tse, Phys. Rev. Lett. **85**, 5130 (2000).
[45] G. Steinle-Neumann, L. Stixrude, and R. E. Cohen, Phys. Rev. B **63**, 054103 (2001).
[46] S. L. Qiu and P. M. Marcus, J. Phys.: Condens. Matter **15**, L755 (2003).
[47] H. P. Klug and L. E. Alexander, *X-Ray Diffraction Procedures for Polycrystalline and Amorphous Materials*, 2nd ed. (Wiley, New York, 1974).
[48] J. I. Langford, J. Appl. Crystallogr. **4**, 164 (1971).
[49] N. Funamori, M. Funamori, R. Jeanloz, and N. Hamaya, J. Appl. Phys. **82**, 142 (1997).
[50] A. K. Singh and C. Balasingh, J. Appl. Phys. **90**, 2296 (2001).
[51] J. F. Kenney and E. S. Keeping, *Mathematics of Statistics*, 3rd ed. (Van Nostrand, Princeton, NJ, 1954).
[52] A. K. Singh, H. P. Liermann, and S. K. Saxena, Solid State Commun. **132**, 795 (2004).
[53] W. R. Panero and R. Jeanloz, J. Appl. Phys. **91**, 2769 (2002).
[54] B. E. Warren, *X-Ray Diffraction* (Addison-Wesley, Reading, MA, 1969).
[55] P. B. Hirsch and H. M. Otte, Acta Crystallogr. **10**, 447 (1957).